



Cite this: *Nanoscale*, 2025, **17**, 13283

## *In situ* synthesis of bimetallic chalcogenides with highly conductive carbon nanotubes for efficient symmetric hybrid supercapacitors†

Soumyajit Jana,<sup>‡a</sup> Sampath Karingula,<sup>‡a</sup> Anjana Sajeevan,<sup>a</sup> Phani Kumar V. V. N.<sup>b</sup> and Yugender Goud Kotagiri  <sup>\*a</sup>

Achieving high energy density and long cycle stability in energy storage devices necessitates excellent electrochemical performance, which often relies on the innovative structural design of the materials under investigation. Therefore, hybrid supercapacitors are crucial in the realm of energy storage devices. The elevated energy and power densities, combined with various energy storage mechanisms, significantly improve electrochemical performance. Here, we developed a highly efficient electrode material, carbon nanotube-metal chalcogenides (CNT-CuNiSe<sub>2</sub>), using a simple one-pot reflux method (*in situ*). The enhanced energy storage performance was achieved by synergising CuNiSe<sub>2</sub> with the pi-cloud of CNTs, resulting in enhanced specific capacitance retention over prolonged cycling stability. The hybrid supercapacitor electrode was formed by combining conducting carbon cloth (CC) with CNT-CuNiSe<sub>2</sub> as a hybrid material, referred to as the CC/CNT-CuNiSe<sub>2</sub> material. The fabricated hybrid electrode materials demonstrated excellent potential for energy storage. CC/CNT-CuNiSe<sub>2</sub> exhibited excellent energy storage capabilities, achieving a specific capacitance of 957.06 F g<sup>-1</sup> at 1 A g<sup>-1</sup>. Hybrid supercapacitors with high energy and power density were developed using conducting carbon cloth and CNT-CuNiSe<sub>2</sub>, designated as CC/CNT-CuNiSe<sub>2</sub>//CC/CNT-CuNiSe<sub>2</sub>. The hybrid capacitor device demonstrated a capacitance of 265.586 F g<sup>-1</sup>, along with an energy density of 82.99 W h kg<sup>-1</sup> at a power density of 1511.35 W kg<sup>-1</sup>. When charged and discharged at 4 A g<sup>-1</sup>, the hybrid capacitor device displayed an impressive capacitance retention of 101.3% over 6000 continuous cycles.

Received 23rd January 2025,

Accepted 27th March 2025

DOI: 10.1039/d5nr00340g

rsc.li/nanoscale

## 1. Introduction

In this 21st century, two major problems are global warming and the energy crisis. Currently, energy production and fuel economy mostly depend on fossil fuels. In this context, energy storage devices and renewable energy sources, such as wind, solar, and hydrogen energy, play a crucial role in meeting the continuous energy demand. Energy storage devices, such as batteries and supercapacitors, are widely employed in modern electronic devices to store electrical energy. Batteries offer high energy density and can power devices throughout the day, typi-

cally requiring an hour to recharge when depleted. However, batteries have relatively shorter lifespans, are often expensive, and can reach high temperatures during ignition or explosion, leading to potential safety risks. For rapid power delivery—characterized by high power density, quick recharge times and the ability to endure a substantial number of cycles (>10<sup>6</sup>)—devices such as capacitors, particularly supercapacitors, are widely employed in smart electronics, electric vehicles, and electromechanical and electrohydrostatic flight control actuation systems.<sup>1</sup> Batteries and supercapacitors differ in their charge storage mechanisms. In lithium-ion batteries, the incorporation of Li ions facilitates redox reactions in the bulk electrode materials, which are governed by diffusion and may occur slowly.<sup>2</sup> Consequently, the charge transfer mechanism in lithium-ion batteries is often limited.

In contrast, supercapacitors (SCs) are energy-storage devices that can store 100 times more charge than traditional capacitors. SCs operate through electrostatic interactions at the electrode/electrolyte interface *via* electrochemical double-layer capacitance (EDLC) or by transferring charge to a layer of redox molecules on the electrode's surface.<sup>3</sup> Therefore, SCs

<sup>a</sup>Department of Chemistry, Indian Institute of Technology Palakkad, Palakkad, Kerala 678 557, India. E-mail: yugenderkotagiri@iitpkd.ac.in

<sup>b</sup>Centre for Automotive Energy Materials, International Advanced Research Centre for Powder Metallurgy and New Materials (ARCI), Chennai 600113, Tamil Nadu, India

† Electronic supplementary information (ESI) available: *In situ* synthesis versus physical mixing synthesis, along with their corresponding XRD and FESEM images of CuNiSe<sub>2</sub>, CNT-NiSe<sub>2</sub>, CNT-CuSe<sub>2</sub>, NiSe<sub>2</sub>, EASA calculations, a table comparing CdI, Cs, and EASA, CV of the three composites at different scan rates, and EIS plots of all the electrodes. See DOI: <https://doi.org/10.1039/d5nr00340g>

‡ Equal contribution.



can provide high power density and energy density for a limited period, making their application different from batteries. It has been noted that Li-ion batteries and supercapacitors have low power and energy densities.<sup>4</sup> To overcome the issues related to the use of metal oxides ( $\text{Co}_3\text{O}_4$ ,  $\text{RuO}_2$ ,  $\text{MnO}_2$ ) in energy storage,<sup>5–7</sup> metal chalcogenides ( $\text{NiSe}_2$ ,  $\text{MoS}_2$ ,  $\text{MoSe}_2$ ,  $\text{CoSe}_2$ )<sup>8–11</sup> have been employed as electrode materials for energy-storage devices, such as supercapacitors, which are best known as pseudo-capacitors. In recent trends, metal chalcogenides have drawn significant attention from researchers and the scientific community due their potential applications in various fields, such as an energy-storage materials, electrocatalysts, and gas sensing.<sup>12–14</sup> Metal selenides (MSe), from the family of metal chalcogenides, have been widely explored and used as electrode materials in both EDLC and pseudo-capacitors. This is due to their inheritance “d” electronic structure, adaptable coordination environment, higher electrical conductivity, low electronegativity, and the participation of filled 3d orbitals of Se and vacant 3d orbitals of metals in electron delocalization. As a result, charge is dispersed around the metal selenides, making them favourable for charge storage applications, such as supercapacitors.<sup>15,16</sup> Monometallic selenides, such as  $\text{NiSe}_2$ , have been notably recognized for their potential in supercapacitor applications.<sup>17</sup> However,  $\text{NiSe}_2$  offers limited energy and power density, and less surface area. Other MSe compounds, including  $\text{CuSe}$  and  $\text{CoSe}_2$ , have also exhibited low energy density, power density, and reduced capacitance retention.<sup>18,19</sup> Therefore, bimetallic and multi-metal selenide (MMSe) compositions, comprising manganese, cobalt, copper, and iron, have been investigated as they may benefit from synergistic effects that can enhance the electrochemical activity beyond the limitations of monometallic compounds.<sup>20,21</sup> For instance,  $\text{CuS}_2@\text{Cu}_7\text{Se}_4@\text{NC}$  was synthesized by Zhu *et al.* and showed high performance for an asymmetric supercapacitor with a capacitance of  $660 \text{ F g}^{-1}$  and density of  $599.7 \text{ W kg}^{-1}$ , while Molaei *et al.* synthesized hollow spheres of  $\text{FeCoSe}_2/\text{NiCoLDH}$  *via* a hydrothermal method, and the composite exhibited a specific capacitance of  $1305 \text{ C g}^{-1}$  and an energy density of  $55.45 \text{ W h kg}^{-1}$ .<sup>22,23</sup> Other examples include  $\text{r-GO/CoNiSe}_2$ , which was synthesized *via* a hydrothermal process by Li *et al.*, and exhibited a specific capacitance of  $2249.7 \text{ F g}^{-1}$  and an energy density of  $143.2 \text{ W h kg}^{-1}$  at  $0.825 \text{ kW kg}^{-1}$  power density, and  $\text{NiSe}_2/\text{MnSe/r-GO}$ , which demonstrated an energy density of  $51.4 \text{ W h kg}^{-1}$  at a power density of  $800.7 \text{ W kg}^{-1}$ , as reported by Q. Lu *et al.* and G. Zhang *et al.*, respectively.<sup>24,25</sup>

Despite their high specific capacitance, a significant problem encountered by pseudo-capacitor materials, such as MSe and MMSe, is their comparatively poor power density compared to EDLCs. This is primarily due to the slower nature of faradaic processes compared to non-faradaic processes. Moreover, pseudo-capacitor electrodes are more susceptible to volumetric alterations during charge and discharge cycles, which can reduce their cycling stability and mechanical integrity.<sup>26</sup> To overcome this issue, hybrid supercapacitors were introduced, combining EDLC and pseudo-capacitors to

provide a large surface area where electrolyte ions can be stored *via* both faradaic and non-faradaic mechanisms. This approach results in enhanced energy density, power density, and long cyclic stability. These hybrid devices typically employ non-faradaic materials, such as carbon-based substances (CNT, GO, CNF, graphite, carbon sponges, and carbon nanosheets), in combination with faradaic materials like metal chalcogenides, metal oxide, conducting polymers, organic redox polymers, and MOF-based substances.<sup>10,27–30</sup> The role of carbon as a support or coating on metal selenide particles is essential in inhibiting their aggregation during the electrochemical process. This is due to the strong electrostatic interaction between carbonaceous materials and metal selenide nanoparticles. Such interactions enhance the electrostatic interaction between the active material and the electrolyte, leading to enhanced electrochemical performance.<sup>10,27</sup> In addition, carbon-based materials are easy to process, low in toxicity, lightweight, and have tunable porosity. In addressing environmental challenges, carbon nanotubes (CNT) have been thoroughly investigated for use in energy storage devices due to their zero-band gap, remarkable electrical conductivity, and mechanical strength. These properties make them ideal for supercapacitors (SCs) and flexible electronic storage. Potential applications of CNTs encompass portable electronic products such as wearables, electronic paper, rollable displays, computing systems, and mobile phones.<sup>31–33</sup>

Numerous synthesis protocols have been developed for the formation of hybrid materials for energy storage, including one-pot synthesis methods such as one-step hydrothermal and wet chemical approaches. For instance, B. G. Amin *et al.* synthesized  $\text{NiCo}_2\text{Se}_4/\text{rGO}$  on Ni foam *via* one-step hydrothermal synthesis at  $145 \text{ }^\circ\text{C}$  for 8 h.<sup>34</sup> Furthermore, there are two other methods commonly used: *in situ* and *ex situ* synthesis. As an example,  $\text{NiCo}_2\text{S}_4$  on carbon cloth was synthesized by Yan *et al.* at  $160 \text{ }^\circ\text{C}$  for 12 h, and the  $\text{CeO}_2/\text{CeS}_2$  nanocomposite was fabricated by Bibi *et al.* using a hydrothermal method.<sup>35,36</sup> All of the above fabrication protocols offer advantages, such as the ability to control the size and morphology of the composite. However, the one-pot method has the disadvantage of providing less control over structural morphology and stability. Although hydrothermal and solvothermal approaches are traditional and widely explored, these methods, despite being controlled synthesis pathways, are not environmentally friendly or cost-effective. And these protocols requires high temperature, high pressure, and long duration for the nanomaterials synthesis.<sup>37–39</sup> In contrast, a simple one-pot synthesis *via* an *in situ* approach using liquid-phase reduction techniques offers an effective alternative for synthesizing bimetallic nanomaterials. This approach is eco-friendly, economical, and essential for controlling the form and size of nanomaterials by adjusting reaction parameters and mole ratios.<sup>40,41</sup>

In this study, we synthesized  $\text{CNT-CuNiSe}_2$  using liquid-phase reduction methods with an *in situ* approach for application in hybrid supercapacitor devices. This electrode exhibited a distinctive electron transport mechanism, ensuring high



energy density and an efficient synthesis process. Furthermore, the physical characterization of CNT-CuNiSe<sub>2</sub> was conducted using FT-IR, Raman spectroscopy, and XRD. The morphology and surface properties of CNT-CuNiSe<sub>2</sub> were analyzed through FESEM, HRTEM, and BET isotherms. Electrochemical studies of all composites were performed using CV, GCD, and EIS techniques with both three-electrode and two-electrode (flat cell) configurations in a 6 M KOH electrolyte. In addition, CNT-CuNiSe<sub>2</sub> demonstrated excellent electrical conductivity and substantial specific capacitance. The CNT-CuNiSe<sub>2</sub>-based device, featuring carbon cloth, demonstrated an energy density of 82.99 W h kg<sup>-1</sup> and the highest power density of 48.25 kW kg<sup>-1</sup>. Additionally, the CNT-CuNiSe<sub>2</sub> device demonstrated enhanced endurance, maintaining performance over 6000 continuous galvanostatic charge and discharge cycles. After 6000 cycles, the CNT-CuNiSe<sub>2</sub> device retained 101.3% of specific capacitance, and demonstrating remarkable coulombic efficiency of 93.6%. This represents the first documented approach for the cost-effective and environmentally friendly synthesis of CNT-CuNiSe<sub>2</sub>, along with the development of 1.5 V electrodes designed for hybrid supercapacitor applications.

## 2. Experimental section

### 2.1 Chemicals and materials

Copper chloride dihydrates (CuCl<sub>2</sub>·2H<sub>2</sub>O), nickel chloride hexahydrate (NiCl<sub>2</sub>·6H<sub>2</sub>O, extra pure, AR, 99%), sodium selenite anhydrous (Na<sub>2</sub>SeO<sub>3</sub>, AR, 99%), sodium borohydride (NaBH<sub>4</sub>), multi-walled carbon nanotubes (MWCNT Type-6, Sigma Aldrich), sulfuric acid (H<sub>2</sub>SO<sub>4</sub>, 99%), nitric acid (HNO<sub>3</sub>, 98%), 5% Nafion solution, isopropyl alcohol, *N*-methyl pyrrolidone (NMP, 99%), conducting carbon cloth (SRL), Super-p carbon, and polyvinylidene fluoride (PVDF) were purchased from The Electrode Store (TES), India.

### 2.2 Synthesis of functionalized CNTs

Multi-walled carbon nanotubes (CNTs) were utilized as supports in our hybrid supercapacitor composite. Before application, the carbon nanotubes (CNTs) underwent functionalization with -COOH groups following the established protocol. Briefly, 500 mg of multi-walled carbon nanotubes (MWCNTs) were uniformly dispersed in 75 ml of 3 M nitric acid (HNO<sub>3</sub>). The solution then underwent sonication for a duration of 5 min, followed by stirring for 22–24 h at a temperature of 60 °C. The resulting black solid suspension was subsequently rinsed gently by centrifuging it several times with Milli-Q water until a neutral pH of 7 was achieved. The obtained black solid was then dried in an oven at 70 °C for 12 h. In this stage, HNO<sub>3</sub> facilitated the oxidation of the CNTs by triggering the development of the -COOH group along the sidewalls and at the ends of the CNT structure. This phenomenon results in effects that subsequently enhance the loading of metal nanoparticles with a uniform distribution. This process of

functionalization can enhance the dispersion of CNTs in catalytic ink by increasing their solubility.<sup>36</sup>

### 2.3. *In situ* synthesis of CNT-CuNiSe<sub>2</sub>

Using the *in situ* approach, CNT-CuNiSe<sub>2</sub> was synthesized. The standard process involved dissolving 0.35 g of NaBH<sub>4</sub> in 100 mL of deionized water. Next, Na<sub>2</sub>SeO<sub>3</sub> powder (0.345 g) was added to the mixture and stirred until total dissolution. Meanwhile, in 100 mL of deionized water, 0.4 g of functionalized CNTs, 0.237 g of NiCl<sub>2</sub>·6H<sub>2</sub>O, and 0.118 g of CuCl<sub>2</sub>·2H<sub>2</sub>O were simultaneously dissolved with the help of a 10 ml disposable syringe. During sample preparation, a continuous nitrogen flow was introduced to prevent the key intermediates from easily oxidizing into high valences during selenium reduction.<sup>42</sup> Nickel and copper salts solutions were introduced to the reaction vessel after a continuous flow of N<sub>2</sub> gas for the 10 minutes, and the solution kept stirring for 2 hours at 90 °C. Scheme 1 illustrates the CNT-CuNiSe<sub>2</sub> synthesis protocol. The black precipitate was separated by centrifugation after stirring, and it was then vacuum-dried for 12 h at 50 °C. Following the same synthesis protocol, we also synthesized Cu<sub>1-x</sub>Ni<sub>x</sub>Se<sub>2</sub>, NiSe<sub>2</sub>, CuSe<sub>2</sub>, CNT-NiSe<sub>2</sub>, and CNT-CuSe<sub>2</sub>, respectively.

### 2.4. Sample preparation for electrochemical characterization

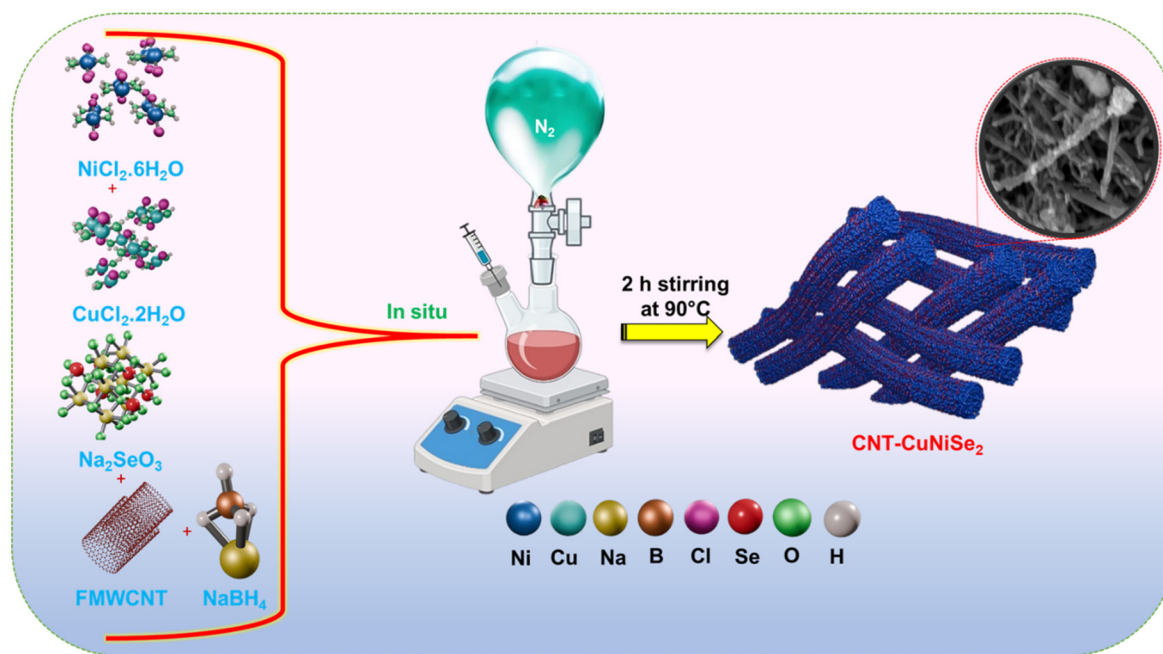
**2.4.1. Three-electrode fabrication.** A glassy carbon electrode (GCE) with a 0.0706 cm<sup>2</sup> surface area was used as the working electrode. The GCE was polished with 0.3 μm alumina suspension and rinsed with water. Catalyst ink was prepared by dissolving 3 mg of composite in binder mixture which contains DI water, IPA, and 5% Nafion with a volume ratio of 4 : 1 : 0.05. The resultant mixture was sonicated for 2 h, at 1 h intervals. Next, 3 μL of the prepared ink was coated twice on the GCE with the help of a micropipette, and the modified electrode was dried overnight at room temperature. The modified GCE was named CNT-CuNiSe<sub>2</sub>.

**2.4.2. Fabrication of the conducting carbon cloth/CNT-CuNiSe<sub>2</sub>.** Two conducting carbon cloths sized 1 × 1 cm<sup>2</sup> were cut and weighed out before coating. For electrode modification, 100 mg of a coating material, consisting of CNT-CuNiSe<sub>2</sub> as the active material, PVDF as a binder, and Super P carbon as the conducting support in a weight ratio of 8 : 1 : 1, was taken followed by the addition of 400 μL of the NMP in a mortar, and then ground well with a pestle for 60 min until a uniform slurry was formed. The black slurry was coated onto the carbon cloth by drop casting, and the coated carbon cloth was dried overnight at 80 °C. The coated cloth was weighed out, and the amount of the CNT-CuNiSe<sub>2</sub> was found to be 0.002 g. The carbon cloth was named as CC/CNT-CuNiSe<sub>2</sub>.

### 2.5. Instrumentation

Morphological analysis of our synthesized materials was performed by field emission electron microscopy (FESEM, Gemini SEM 300, 15 kV) and HRTEM (HEOL, JAPAN, JEM-2100 Plus), and the images were processed by ImageJ software. The composition of the materials was assessed by elemental mapping





Scheme 1 Schematic of the *in situ* synthesis of CNT-CuNiSe<sub>2</sub>.

utilizing energy-dispersive X-ray (EDX) spectroscopy. X-Ray diffraction (XRD) patterns were obtained using Rigaku XRD Smart Lab system in the range of 20° to 90°. FT-IR spectra were recorded in the range of 400–4000 cm<sup>-1</sup> using an FT-IR instrument from Shimadzu Scientific Instruments. To determine the crystal structure, a Raman spectrophotometer (Horiba Labram HR Evo) was employed. Brunauer–Emmett–Teller (BET) analysis was done on a surface area analyzer from Quantachrome.

## 2.6. Electrochemical characterization

Electrochemical characterization was performed with the help of cyclic voltammetry (CV), galvanostatic charge and discharge (GCD), and electrochemical impedance spectroscopy (EIS) on a potentiostat/galvanostat (Model 6054e, CH instrument, USA). The three-electrode setup was established utilizing a GCE with a working area of 0.0706 cm<sup>-2</sup>, Hg/HgO in 1 M KOH as the reference electrode, and Pt wire as the counter electrode, all immersed in 6 M KOH electrolyte. In the two-electrode setup, the cathode and anode were made of the same materials. Electrochemical impedance spectroscopy (EIS) was performed utilizing a sinusoidal alternating frequency spanning from 0.01 Hz to 10<sup>5</sup> Hz, accompanied by an amplitude of 5 mV and a steady direct current bias potential of 0.3 V.

## 3. Results and discussion

### 3.1 Material characterization

The one-pot synthesis method serves as a clear and efficient approach that maximizes time and energy resources. This established method integrates the precursors for both

materials into a unified reaction, enabling the simultaneous synthesis of two materials and the formation of hybrid structures in a single step. Additionally, the *in situ* synthesis of TMC-based hybrids is a frequently studied approach, as it promotes effective interfacial interactions and allows for direct control over the morphologies. In this approach, one component serves as a structural backbone, while its counterpart undergoes nucleation and growth on the backbone. Taking advantage of this method, an *in situ* approach was employed here in a one-pot synthesis to produce the CNT-CuNiSe<sub>2</sub> composite using a liquid-phase reduction method, as schematically shown in Scheme 1. In this process, functionalized multi-walled carbon nanotubes (MWCNTs) were added to the reaction vessel along with Ni and Cu salts, Se sources, and NaBH<sub>4</sub> as reducing agent in an aqueous medium under inert conditions. The functionalized MWCNTs' surfaces were coated with CuNiSe<sub>2</sub>, resulting in the formation of the CNT-CuNiSe<sub>2</sub> composite. We then tested the energy-storage performance of the CNT-CuNiSe<sub>2</sub>, which showed satisfactory results.

FT-IR is a useful technique for characterizing CNT-based monometallic and bimetallic selenide materials at the preliminary stage. We developed a green approach for the synthesis of our materials *via* an *in situ* reaction and liquid-phase reduction methods in one pot. In this one-pot process, CNTs and an equimolar ratio of Cu and Ni salts were added, resulting in the desired CNT-CuNiSe<sub>2</sub> product. In Fig. 1(a), peaks corresponding to the –C=C bond at 1636 cm<sup>-1</sup>, –M–Se bond in the 700–650 cm<sup>-1</sup> range, and a broad peak in the 3400–3200 cm<sup>-1</sup> range due to –O–H groups were observed. These peaks were also observed for CNT-NiSe<sub>2</sub> and CNT-CuSe<sub>2</sub>.<sup>43</sup> Raman spectra was recorded in the 400 to 2000 cm<sup>-1</sup> range and shown in Fig. 2(b). The spectrum showed two characteristic peaks at



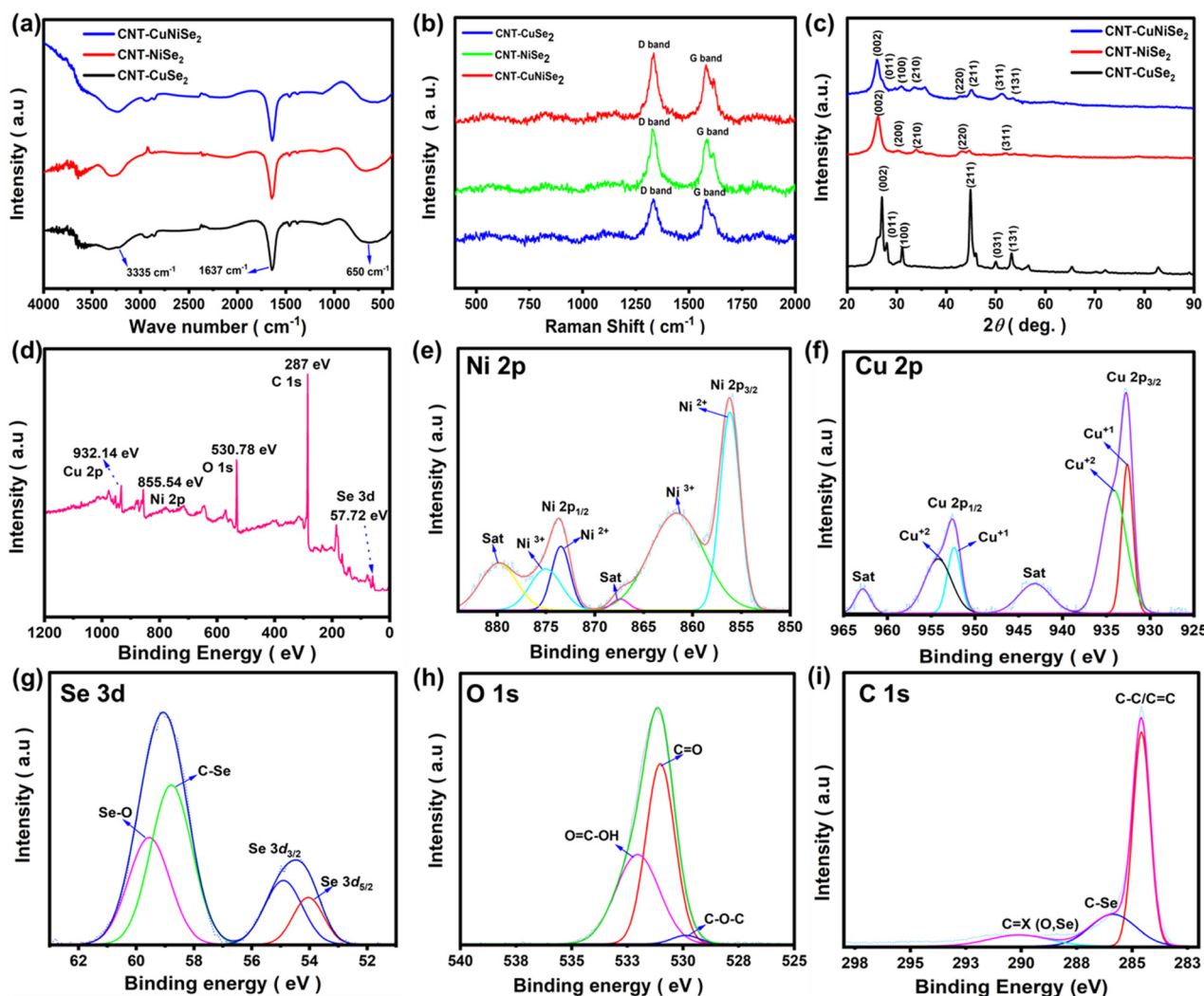


**Fig. 1** (a) FT-IR spectra of CNT-CuNiSe<sub>2</sub>, CNT-NiSe<sub>2</sub>, and CNT-CuSe<sub>2</sub>. (b) Raman spectra of CNT-CuNiSe<sub>2</sub>, CNT-NiSe<sub>2</sub>, and CNT-CuSe<sub>2</sub>. (c) XRD patterns of CNT-CuNiSe<sub>2</sub>, CNT-NiSe<sub>2</sub>, and CNT-CuSe<sub>2</sub>. (d) XPS survey spectrum of CNT-CuNiSe<sub>2</sub> and high-resolution XPS spectra of (e) Ni 2p, (f) Cu 2p, (g) Se 3d, (h) O 1s, and (i) C 1s.

around 1300–1400  $\text{cm}^{-1}$ , corresponding to the D band. This peak was attributed to structural defects in the walls of the nanotubes. Another peak corresponding to the G band was observed at 1500–1600  $\text{cm}^{-1}$ , which was related to the structural vibration of carbon atoms in the graphene layer for all three composites.<sup>44</sup> The  $I_D/I_G$  ratio for CNT-CuNiSe<sub>2</sub> was 1.0101, while for CNT-NiSe<sub>2</sub> and CNT-CuSe<sub>2</sub>, the ratios were 1.0086 and 1.00041, respectively. This indicated that the enhancement of the D band in CNT-CuNiSe<sub>2</sub> could be attributed to the defects and vacancies created by acid treatment and the incorporation of Cu and Ni with the CNTs.<sup>40</sup> Fig. 1(c) shows the XRD diffraction peaks of the synthesized energy materials. The pure crystalline CuSe<sub>2</sub> diffraction peaks (corresponded to JCPDS card No. 01-082-0446) are observed at  $2\theta$  values of 27.99, 44.88, 50.03 and 53.30 are correspond to different phase planes of (011), (020), (221), (031), and (131), respectively.<sup>41</sup> The (200), (210), (220), and (311) planes corre-

sponding to  $2\theta$  values of 30.27°, 33.54°, 51.26°, and 61.68° belonged to the cubic NiSe<sub>2</sub> structure (JCPDS 88-1711).<sup>45</sup> In CNT-CuNiSe<sub>2</sub>, the XRD diffraction pattern was assigned to a combination of Ni and Cu peaks, indicating that they adopted the same crystal structure, as no additional peaks were observed. Furthermore, a peak around 26.23° corresponded to the (002) diffraction of the CNT.<sup>46</sup> The SEAD pattern from HRTEM analysis supported the XRD diffraction pattern, and the lattice spacing between the crystal planes was calculated from TEM studies, as shown in Fig. 3.

Further, XPS studies were conducted to describe the electronic arrangements of the CNT-CuNiSe<sub>2</sub> composite. The X-ray survey spectrum confirmed the presence of Ni, Cu, Se, O, and C elements at binding energies of 855.54, 932.14, 57.72, 287, and 530.76 eV, respectively, as illustrated in Fig. 1(d). The high-resolution XPS data for Ni 2p, shown in Fig. 1(e), revealed Ni<sup>2+</sup> peaks at 854.4 and 871.7 eV, while peaks at 855.7 and



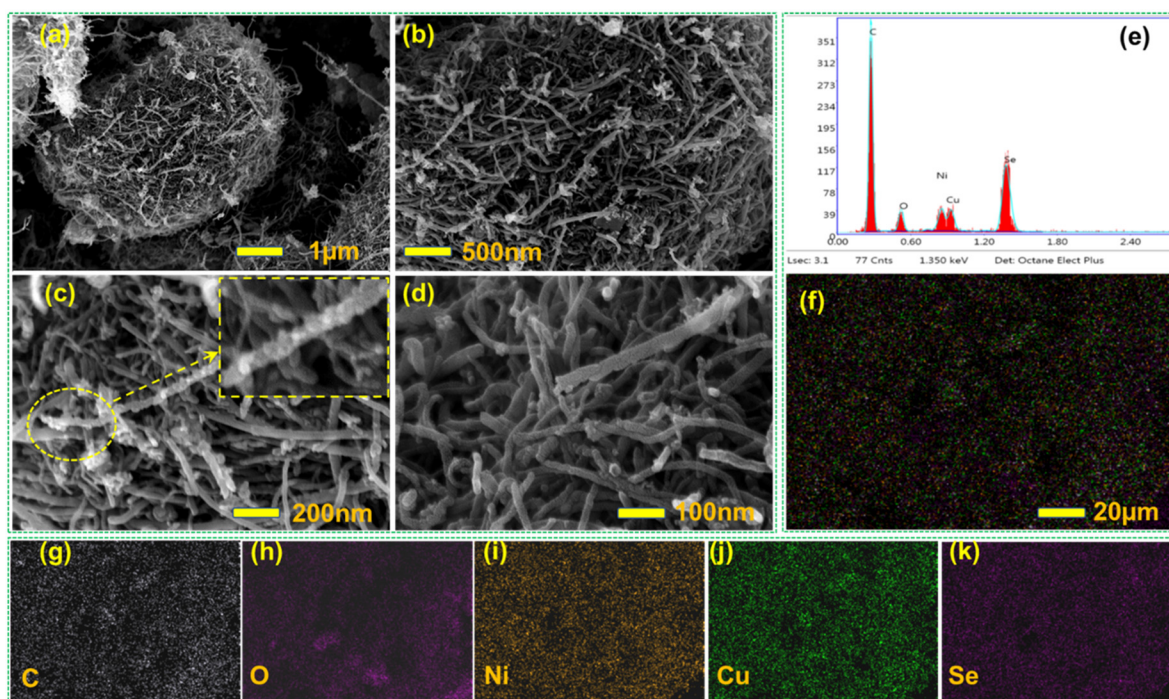


**Fig. 2** (a)–(d) FESEM images of the CNT-CuNiSe<sub>2</sub> at different magnifications. (e) EDX spectrum, (f) EDX elemental mapping, and maps for the corresponding elements (g) C, (h) O, (i) Ni, (j) Cu, and (k) Se.

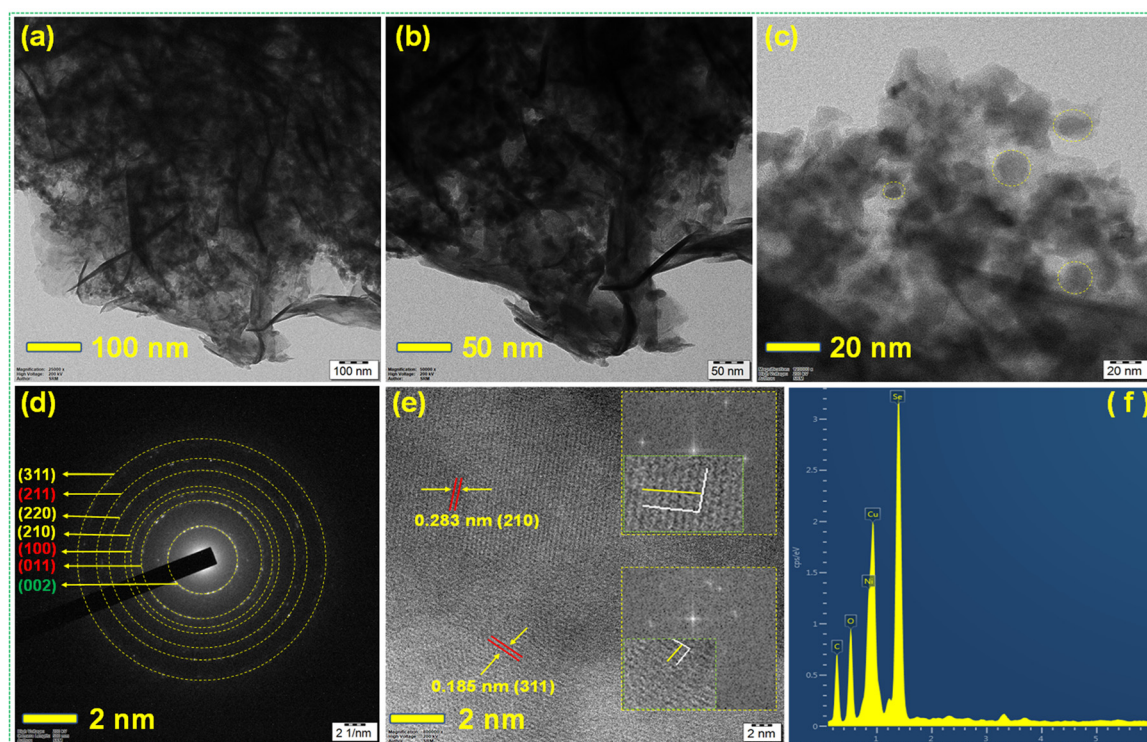


**Fig. 3** (a), (b) and (c) HRTEM images of the CNT-CuNiSe<sub>2</sub> at different magnifications. (d) SAED pattern of CNT-CuNiSe<sub>2</sub>. (e) High-resolution image of the CNT-CuNiSe<sub>2</sub> composite and corresponding IFFT profiles of lattice spacing shown as insets. (f) EDS analysis of CNT-CuNiSe<sub>2</sub>.



873.4 eV indicated the presence of  $\text{Ni}^{3+}$  in CNT-CuNiSe<sub>2</sub>. Satellite peaks were also observed at 864 and 880 eV for the Ni 2p<sub>3/2</sub> and Ni 2p<sub>1/2</sub> species, respectively.<sup>47</sup> Fig. 1(f) displays a high-resolution spectrum of Cu 2p, showing six peaks upon deconvolution. The peaks at 932.66 and 952.55 eV were indicative of the Cu<sup>1+</sup> state, while peaks at 934.247 and 954.21 eV corresponded to the Cu<sup>2+</sup> state in CNT-CuNiSe<sub>2</sub>.<sup>48</sup> Furthermore, two satellite peaks were detected at 943.27 and 962.79 eV. These findings provide evidenced that the formation of bimetallic selenides and the presence of multiple redox couples contributed to an increased electrochemical storage capacity. The oxidation state of selenium was determined through X-ray photoelectron spectroscopy (XPS) analysis. The spectrum exhibited significant peaks at 54.06, 55.05, 58.75, and 59.59 eV, corresponding to Se3d<sub>5/2</sub>, Se3d<sub>3/2</sub>, C–Se, and oxidized S–O, respectively. This indicated that selenium was primarily in the Se<sup>2–</sup> state, with both bonded and elemental selenium also present, as illustrated in Fig. 1(g).<sup>49–51</sup> Additionally, the O 1s spectrum in Fig. 1(h) exhibited peaks at 532.02, 531.01, and 529.77, corresponding to O=C–OH, C=X (where X = O, Se), and C–O–C, respectively.<sup>52</sup> The C 1s XPS spectrum exhibited peaks at 284.85 eV for C=C/C–C, 285 eV for C–Se, and 288.96 eV for C=X (O, Se), as shown in Fig. 1(i).<sup>53</sup> Furthermore, the XPS elemental spectrum (Fig. 1) aligned closely with the EDX elemental data obtained from the SEM analysis (Fig. 2).

SEM and TEM were performed to characterize the materials' morphology and structure. As shown in the FESEM images in Fig. 2(a) and (d) at various magnifications (ranging from 1 μm to 100 nm), the spherical CuNiSe<sub>2</sub> nanoparticles were uniformly distributed over the walls of the MWCNTs, confirming the formation of CNT-CuNiSe<sub>2</sub>. The carbon nanotubes supported the CuNiSe<sub>2</sub> nanoparticles. EDX elemental mapping confirmed the presence of C, O, Ni, Cu, and Se, with peaks shown in Fig. 2(e) and (f). The distribution of elements in the composite is shown in Fig. 2(g)–(k). Further, the ICP-OES analysis was performed to determine the actual contents of Ni, Cu, and Se in the CNT-CuNiSe<sub>2</sub> hybrid composite. The result showed that the CNT-CuNiSe<sub>2</sub> composite contained Ni (101.2 g kg<sup>–1</sup>), Cu (102.4 g kg<sup>–1</sup>), and Se (115.4 g kg<sup>–1</sup>). The corresponding bar diagram is shown in the ESI (Fig. S1†). Fig. S2(a) and (b)† illustrate the distinct morphologies observed during composite synthesis *via in situ* synthesis in a single pot, where all the composites were introduced simultaneously under an inert atmosphere. In contrast, physical mixing methods were also explored, wherein MMSe and CNT were combined in a pot without inert conditions and subjected to sonication for the synthesis of CNT-CuNiSe<sub>2</sub>. *In situ* synthesis in a single pot demonstrated morphological benefits compared to the physical mixing approach, as supported by the XRD diffraction peaks shown in Fig. S2(c).† The SEM images of CuNiSe<sub>2</sub> in Fig. S3(a) and (b)† provide a clear picture of sphere-like nanoparticles and pores in the composite. Similarly, for CNT-NiSe<sub>2</sub> and CNT-CuSe<sub>2</sub>, SEM images were taken in the range of 1 μm to 100 nm and depicted that NiSe<sub>2</sub> and CuSe<sub>2</sub> were also well distributed, similar to CuNiSe<sub>2</sub>, in

the CNT walls, as shown in Fig. S4(a)–(d) and S5(a)–(d).† No significant morphological changes were observed in the bimetallic selenides and monometallic selenides, as shown in Fig. S6(a) and (b)† for NiSe<sub>2</sub>.

Next, high-resolution transmission electron microscopy (HRTEM) was utilized for additional morphological analysis, as shown in Fig. 3. The HRTEM images of CNT-CuNiSe<sub>2</sub> at various magnifications, as illustrated in Fig. 3(a)–(c), revealed the presence of flat, smooth surfaces and irregular, sphere-like nanoparticles dispersed across the CNT walls, as corroborated by the FESEM images. The sizes of the individual CNT-CuNiSe<sub>2</sub> spheres ranged from 11 to 23 nm. Scaled selected area electron diffraction (SAED) images of the spheres were obtained to determine the material phase by measuring the lattice spacing and by comparing the results with standard X-ray diffraction (XRD) data. In Fig. 3(d), the SEAD pattern (002) in green corresponds to the CNT planes (011) and (100), and the (211) in red to CuSe<sub>2</sub>, while the remaining planes (210), (220), and (311) in yellow are associated with NiSe<sub>2</sub>. The inverse fast Fourier transform (IFFT) analysis yielded *a* lattice *d* spacing value of 0.283 nm for the (210) plane and 0.185 nm for the (311) plane. The EDS of CNT-CuNiSe<sub>2</sub> revealed the presence of various elements in this composite, with the results aligning closely with those from the EDS and XPS analyses.

The surface area, pore size, and pore volume are essential factors that can influence the energy-storage performance of a supercapacitor. For instance, hybrid composites typically exhibit an increased surface area, leading to a higher observed capacitance. Furthermore, a composite with a reduced pore size and narrower dimensions will result in a pore volume distribution that enhances the energy density. Thus, choosing a microporous composite is optimal for supercapacitor composites, while a mesoporous structure offers a greater specific surface area. Therefore, hybrid materials that possess both microporous and mesoporous characteristics represent the optimal choice for hybrid supercapacitor composites.<sup>54,55</sup>

The BET isotherm and porosity of the CNT-CuNiSe<sub>2</sub>, CNT-NiSe<sub>2</sub>, and CNT-CuSe<sub>2</sub> were analyzed by performing BET N<sub>2</sub> adsorption–desorption isotherms, as shown in Fig. 4(a). The surface areas of CNT-CuNiSe<sub>2</sub>, CNT-NiSe<sub>2</sub> and CNT-CuSe<sub>2</sub> were 64, 62.27 and 49.15 m<sup>2</sup> g<sup>–1</sup>, respectively. It was observed that the multi-metal CuNiSe<sub>2</sub> with CNTs had a greater surface area compared to the monometallic NiSe<sub>2</sub> and CuSe<sub>2</sub> with CNTs. The DFT method revealed the pore size and pore volume distribution and cumulative surface area of all the three composites, which were shown in Fig. 4(b)–(d). N<sub>2</sub> adsorption analysis at 77.350 K under a relative pressure range of 0.0000–1.0000 was performed with the help of the non-local density functional theory (NCDFT) equilibrium model. The analysis indicated that all the composites had a porous nature, with most of the pore volume populated primarily between a 2–25 nm pore width. Among all the composites, CNT-CuNiSe<sub>2</sub> exhibited the maximum active surface area with a pore width of ≤5 nm, covering 25 m<sup>2</sup> g<sup>–1</sup> (≈49%) out of the total active surface area of 51.06 m<sup>2</sup> g<sup>–1</sup>. Meanwhile CNT-NiSe<sub>2</sub> covered 27.02 m<sup>2</sup> g<sup>–1</sup> (≈54.42%) out of 49.08 m<sup>2</sup> g<sup>–1</sup>, while CNT-CuSe<sub>2</sub>



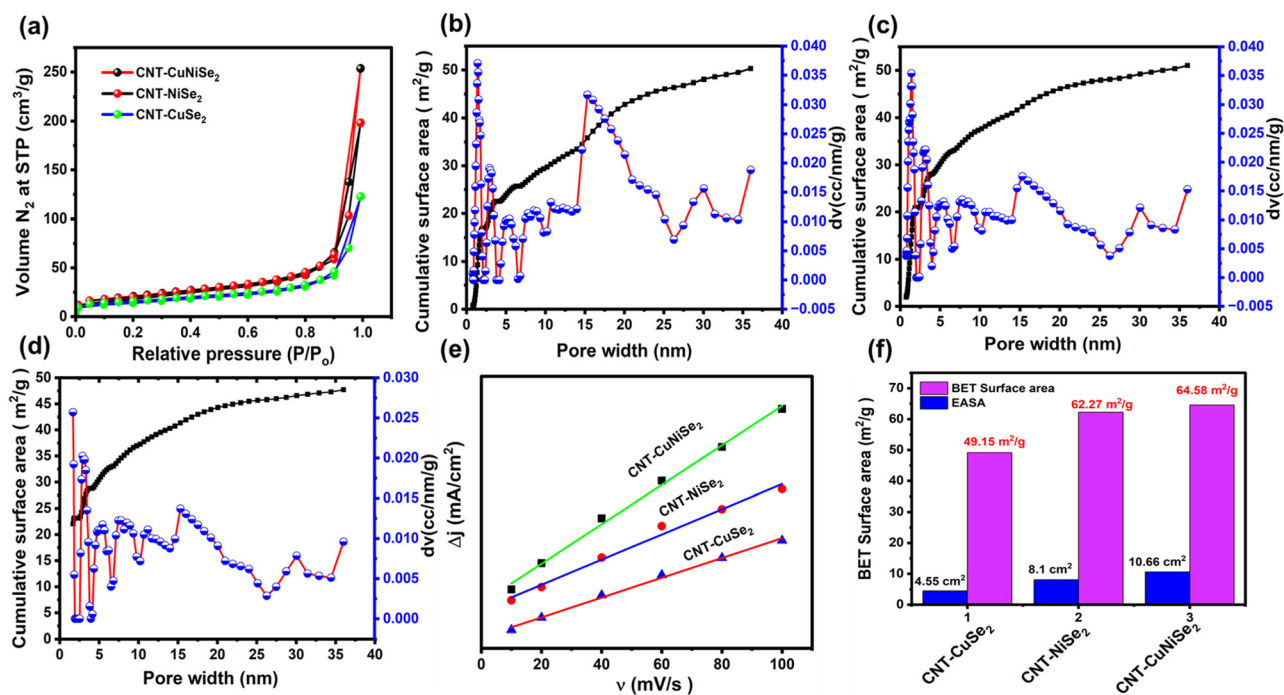


Fig. 4 (a) BET isotherms of CNT-CuNiSe<sub>2</sub>, CNT-NiSe<sub>2</sub>, and CNT-CuSe<sub>2</sub>. (b–d) Plots of the cumulative surface area versus pore volume against the pore distribution. (e) Double-layer capacitances of the composites from non-faradaic CV after linear fitting. (f) BET surface area plot against the EASA of all three composite materials.

covered less surface area with a pore width  $\leq 5$ . Within the  $\leq 25$  nm region, CNT-CuNiSe<sub>2</sub> possessed  $45.2 \text{ m}^2 \text{ g}^{-1}$  (88.52%), but the other two composites showed less surface area in this pore width. These surface area values were found to be nearly equal to those reported in the existing literature.<sup>56,57</sup> Furthermore, the combination of both a microporous and mesoporous nature helped CNT-CuNiSe<sub>2</sub> to achieve a high specific capacitance. For the percolation and unrestricted flow of ions and substrates at the electrode–electrolyte interface, nanopores with a diameter of less than 5 nm and mesopores with a breadth of less than 25 nm will work well. Thus, the presence of microporosity in CNT-CuNiSe<sub>2</sub> could support achieving a higher charge-storage capacity among all the other composites. The active surface area and electrochemical active surface area (EASA) of these materials were calculated by using BET and cyclic voltammetry (CV), respectively. Here, EASA and double layer capacitance (Cdl) were calculated by taking non-faradaic region current values of the voltammograms of three composites which were shown in Fig. S6 (a)–(c).† The plots of the specific current density vs. scan rate for all the electrodes are shown in Fig. S6,† and the double-layer capacitance of each electrode was evaluated from these plots. CNT-CuNiSe<sub>2</sub>, CNT-NiSe<sub>2</sub>, and CNT-CuSe<sub>2</sub> showed capacitance values of 0.373, 0.285 and 0.1593  $\text{mF cm}^{-2}$ , with the results showing that CNT-CuNiSe<sub>2</sub> provided a high capacitive value, as depicted in Fig. 4(e). The capacitance values were directly proportional to the EASA, with the EASA calculated using the formula  $\text{EASA} = C_{\text{dl}}/C_s$ , as shown in Fig. S7.† Fig. 4(f) shows the values for

the EASA and BET surface area for the three materials, with CNT-CuNiSe<sub>2</sub> showing the highest results in both cases, indicating that it had more surface area available for electrochemical reaction and offered enhanced energy-storage performance.

### 3.2. Electrochemical characterization

Before developing the hybrid supercapacitor, we assessed the supercapacitive performance of the synthesized samples using a three-electrode cell configuration. This assessment sought to validate the suitability of our materials for their intended application in supercapacitor devices. It has been reported that the specific conductivity of a 6 M KOH solution ( $62.66 \times 10^{-2} \text{ S cm}^{-1}$ ) surpasses that of lower concentrations (1 to 5 M), demonstrating enhanced effectiveness for improving supercapacitive properties.<sup>55,56</sup> Consequently, 6 M KOH solution was chosen as the electrolyte for this investigation, and concentrations exceeding 6 M were intentionally avoided due to their tendency to cause the aggregation of electroactive materials from the electrode surface.<sup>56</sup> Initially, the electrochemical studies were done for MMSe, such as CuNiSe<sub>2</sub>, and MSe, such as NiSe<sub>2</sub> and CuSe<sub>2</sub>. The studies depicted that CuNiSe<sub>2</sub> showed better electrochemical activity in the CV analysis, as presented in Fig. S8(a),† and a higher charge-storage capacity as the discharge time was higher in the GCD analysis, whereas NiSe<sub>2</sub> and CuSe<sub>2</sub> displayed a lower current density and lower discharge time, as shown in Fig. S8(b).† Before conducting the electrochemical analysis of CNT-CuNiSe<sub>2</sub>, CNT-NiSe<sub>2</sub>, and

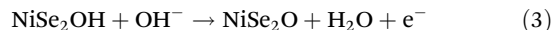


CNT-CuSe<sub>2</sub>, the study also examined the electrochemical performance of Cu<sub>1-x</sub>Ni<sub>x</sub>Se<sub>2</sub> with various molar ratios of Cu and Ni, without the presence of CNTs. Cyclic voltammetry at 20 mV within the range of -0.2 to 0.65 V was conducted, revealing that equimolar ratios of Cu and Ni yielded the highest current density, as illustrated in Fig. 5(a). Additionally, multiple redox couple behaviours were noted across all cases, with the intensity of Cu<sub>0.5</sub>Ni<sub>0.5</sub>Se<sub>2</sub> exhibiting the highest peak current. Additionally, the charge and discharge times of Cu<sub>0.5</sub>Ni<sub>0.5</sub>Se<sub>2</sub> were improved in the GCD analysis, as illustrated in Fig. 5(b). This finding was strongly corroborated by the CV investigation, which ruled out all other composites except Cu<sub>0.5</sub>Ni<sub>0.5</sub>Se<sub>2</sub>. To enhance the electrochemical performance, carbon nanotubes were incorporated into Cu<sub>0.5</sub>Ni<sub>0.5</sub>Se<sub>2</sub>, NiSe<sub>2</sub>, and CuSe<sub>2</sub>, resulting in the composite CNT-CuNiSe<sub>2</sub>, CNT-NiSe<sub>2</sub>, and CNT-CuSe<sub>2</sub>. Cyclic voltammetry was next conducted to assess their electrochemical behaviour, with the corresponding CV profiles analyzed at 20 mV s<sup>-1</sup> within the range of -0.2 V to 0.65 V. CNT-CuNiSe<sub>2</sub> exhibited the highest peak current and a significantly larger enclosed area in the graph compared to all the other electrodes, as indicated by the green peaks in Fig. 5(c). The charge-storage phenomenon was further supported by this discovery, which verified its quasi-reversible redox function. For extra proof, the GCD profile of every electrode was measured at 1 A g<sup>-1</sup>. As shown in Fig. 5(d), the

CNT-CuNiSe<sub>2</sub> discharge duration was noticeably greater than that of CNT-NiSe<sub>2</sub>, CNT-CuSe<sub>2</sub>, CuNiSe<sub>2</sub>, NiSe<sub>2</sub>, and CuSe<sub>2</sub>.

Additionally, three-electrode configurations were used to evaluate CNT-CuSe<sub>2</sub>, CNT-NiSe<sub>2</sub>, and CNT-CuNiSe<sub>2</sub> in 6 M KOH solution. According to the results of this study, CNT-CuNiSe<sub>2</sub> exhibited superior electrochemical performance for the hybrid SC materials. For the CNT-CuSe<sub>2</sub> and CNT-NiSe<sub>2</sub> electrodes that were first created and evaluated, Fig. 6(a) and (b) show that CNT-CuSe<sub>2</sub> had a lower current density and a shorter discharge time; whereas CNT-NiSe<sub>2</sub> showed a sharp, higher peak current and long discharging time, as present in Fig. 6(c) and (d), due to its more active surface area, as revealed by the BET studies.

It is worth noting that CNT-CuNiSe<sub>2</sub> exhibited a larger CV integrated peak area and higher and broader redox intensity peak in Fig. 6(e), due to its multiple redox couples, such as Cu<sup>+</sup>/Cu<sup>2+</sup> and Ni<sup>2+</sup>/Ni<sup>3+</sup>, with eqn (1)–(3) indicating that higher capacity values could be expected from CNT-CuNiSe<sub>2</sub>.<sup>58,59</sup>



The fast movement of electrons and ions at the interface between CNT-CuNiSe<sub>2</sub> and KOH was indicated by the notable

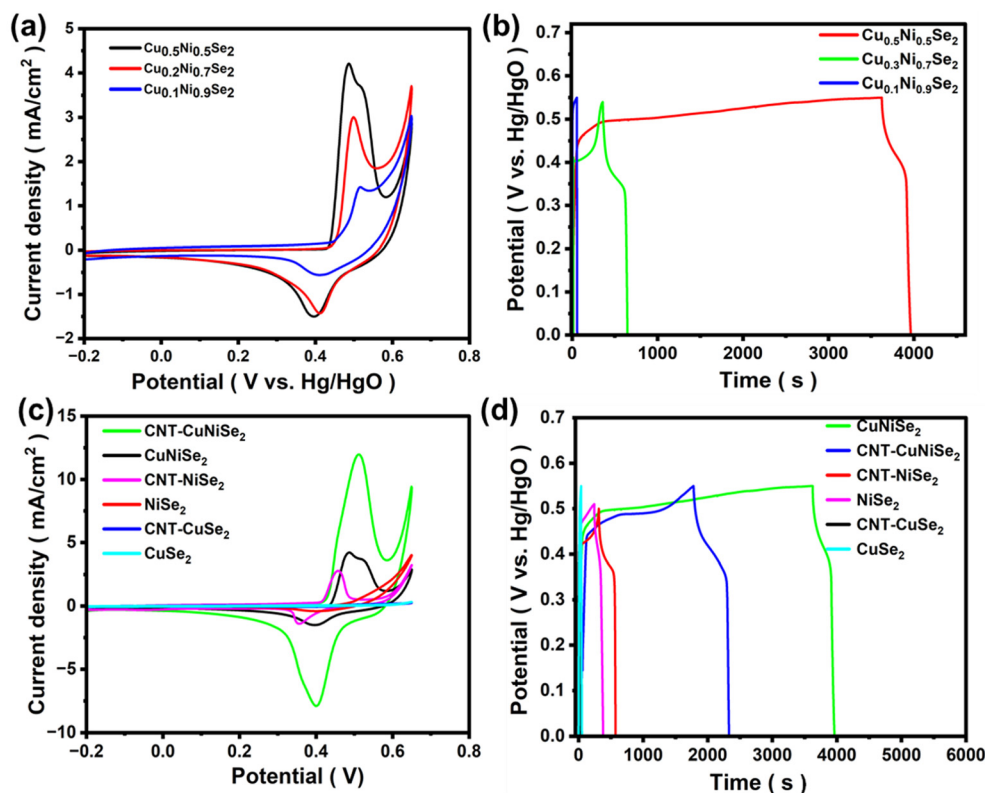
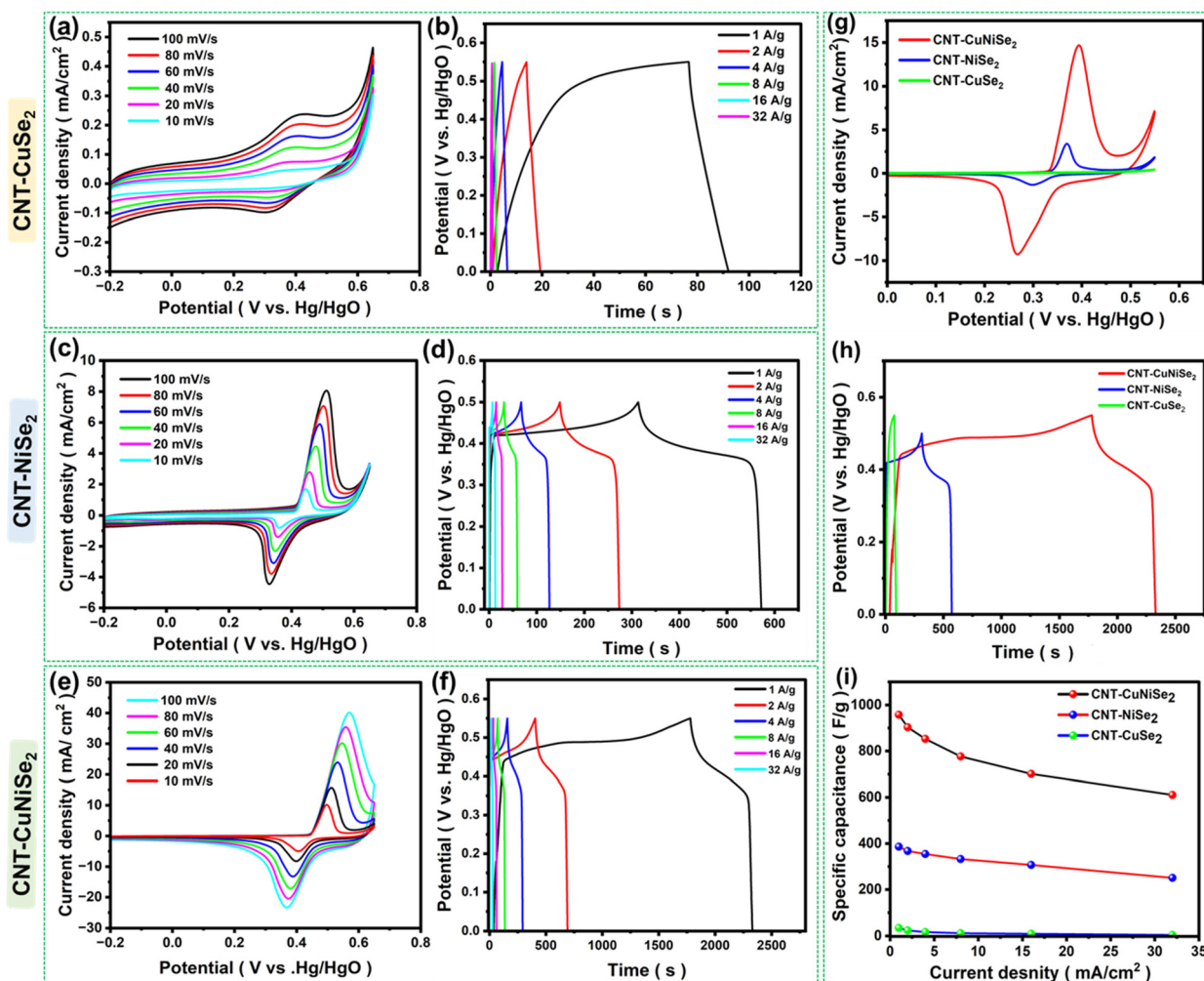


Fig. 5 (a) Comparison of cyclic voltammograms of different compositions of Cu<sub>1-x</sub>Ni<sub>x</sub>Se<sub>2</sub> at 20 mV scan rate. (b) Charging and discharging (GCD) measurements of Cu<sub>1-x</sub>Ni<sub>x</sub>Se<sub>2</sub> at 1 A g<sup>-1</sup>. (c) and (d) Comparison of the CV curves at a 20 mV scan rate and GCD with current densities from 1 to 32 A g<sup>-1</sup> for CuNiSe<sub>2</sub>, NiSe<sub>2</sub>, and CuSe<sub>2</sub>, including CNT-CuNiSe<sub>2</sub>, CNT-NiSe<sub>2</sub>, and CNT-CuSe<sub>2</sub> at various current densities.





**Fig. 6** (a) and (b) CVs and GCD of CNT-CuSe<sub>2</sub> at different scan rates and various current densities from 1 to 32 A g<sup>-1</sup>. (c), (d), (e) and (f) CVs and GCD of CNT-NiSe<sub>2</sub>, CNT-CuNiSe<sub>2</sub> electrodes in 4 M KOH solution from 10 to 100 mV scan rates and at different current densities. (g) CV patterns of CNT-CuNiSe<sub>2</sub>, CNT-NiSe<sub>2</sub>, and CNT-CuSe<sub>2</sub> at 20 mV. (h) Comparison of the GCD at 1 A g<sup>-1</sup> for CNT-CuNiSe<sub>2</sub>, CNT-NiSe<sub>2</sub>, and CNT-CuSe<sub>2</sub> electrodes. (i) Specific capacitance vs. current densities for the CNT-CuNiSe<sub>2</sub>, CNT-NiSe<sub>2</sub>, and CNT-CuSe<sub>2</sub> electrodes.

rise in the current density of all the CVs between 10 and 100 mV s<sup>-1</sup>. In addition, Fig. 6(f) shows that the discharge time of CNT-CuNiSe<sub>2</sub> was much longer than that of CNT-NiSe<sub>2</sub> and CNT-CuSe<sub>2</sub>, suggesting that CNT-CuNiSe<sub>2</sub> performed better in terms of specific capacity. Fig. 6(g) shows the comparison of the CV curves all three electrodes at 20 mV s<sup>-1</sup>. When examined at 1 A g<sup>-1</sup> in Fig. 6(h), the GCD patterns of CNT-CuNiSe<sub>2</sub>, CNT-NiSe<sub>2</sub>, and CNT-CuSe<sub>2</sub> showed prolonged charge and discharge times. The GCD profiles were used to measure the specific capacitance ( $C_s$ ) using eqn (4).

$$C_s = (I \times dt) / m \times dV \quad (4)$$

Upon analysis at 1, 2, 4, 8, 16, and 32 A g<sup>-1</sup>, the  $C_s$  values of CNT-CuNiSe<sub>2</sub> were 957.06, 902.87, 852.86, 776.47, 700.96 and 610.56 F g<sup>-1</sup>, respectively. Further, the same values were 385.96, 367.077, 354.37, 332.25, 306.78 and 250.59 F g<sup>-1</sup>, respectively, for CNT-NiSe<sub>2</sub>. Lastly, measurements of the  $C_s$  of CNT-CuSe<sub>2</sub> revealed that they were 34.73, 23.78, 16.63, 11.75, 9.5 and 4.2 F

g<sup>-1</sup>, respectively. Fig. 6(i) displays plots of the  $C_s$  values of all three materials against various current densities. Because of their superior electrical conductivity, CNTs may help lower the internal resistance, as shown by the enhanced electrochemical activity. CNTs are notable for their abundance of charge-transfer routes, which can speed up Faraday redox reactions.

### 3.3. Two-electrode hybrid symmetric supercapacitor devices

The storage capabilities of the synthesized CNT-CuSe<sub>2</sub>, CNT-NiSe<sub>2</sub>, and CNT-CuNiSe<sub>2</sub> materials, which were coated onto conducting carbon cloth to form electrodes, were evaluated. The resulting configurations, namely, CC/CNT-CuSe<sub>2</sub>, CC/CNT-NiSe<sub>2</sub>, and CC/CNT-CuNiSe<sub>2</sub>, were assembled with a separator and immersed in 6 M KOH, and designated as CC/CNT-CuSe<sub>2</sub>//CC/CNT-CuSe<sub>2</sub>, CC/CNT-NiSe<sub>2</sub>//CC/CNT-NiSe<sub>2</sub>, and CC/CNT-CuNiSe<sub>2</sub>//CC/CNT-CuNiSe<sub>2</sub>, respectively. The symmetric electrodes were examined within an airtight flat cell holder to mitigate air contamination and exposure. The CV



optimization was documented at various scan rates. The optimal potential windows for the hybrid symmetric electrodes, *i.e.*, CC/CNT-CuSe<sub>2</sub>//CC/CNT-CuSe<sub>2</sub>, CC/CNT-NiSe<sub>2</sub>//CC/CNT-NiSe<sub>2</sub>, and CC/CNT-CuNiSe<sub>2</sub>//CC/CNT-CuNiSe<sub>2</sub>, were determined to be 0 to 1.1 V, 0 to 1.4 V, and 0 to 1.5 V, respectively. The cyclic voltammograms at varying scan rates are presented in Fig. 7(a), (c) and (e). The GCD profiles for all three electrodes were analyzed at varying current densities, as illustrated in Fig. 7(b), (d) and (f). Fig. 7(g) compares the CV profiles for all electrodes at a scan rate of 20 mV s<sup>-1</sup>.

The CC/CNT-CuNiSe<sub>2</sub>//CC/CNT-CuNiSe<sub>2</sub> electrode gives the highest background current with redox peaks compared to the two other electrodes. The resulting peaks revealed that the composite contained both EDLC and pseudo-capacitor behaviours. This was attributed to the contributions from both the cathode (CC/CNT-CuNiSe<sub>2</sub>) and anode (CC/CNT-CuNiSe<sub>2</sub>) materials. Significantly, even with elevating the sweep rate, the

integrity of the graphs was maintained, underscoring the device's reversibility and strong electrochemical characteristics. The GCD profiles of the symmetric cells gave quasi-rectangular shapes, and the GCD patterns were compared at 1 A g<sup>-1</sup>, as shown in Fig. 7(h). CC/CNT-CuNiSe<sub>2</sub>//CC/CNT-CuNiSe<sub>2</sub> provided lower Ohmic drops, and the *C<sub>s</sub>* values of all three cells were calculated using eqn (5)

$$C_s = (2 \times (i/m) \times \Delta t) / \Delta V. \quad (5)$$

The *C<sub>s</sub>* values of the CC/CNT-CuNiSe<sub>2</sub>//CC/CNT-CuNiSe<sub>2</sub> cell were measured as 265.586, 209.022, 167.72, 112.0236, 39.68 and 4.096 F g<sup>-1</sup> at 1, 2, 4, 8, 16, and 32 A g<sup>-1</sup>. The *C<sub>s</sub>* values of the CC/CNT-NiSe<sub>2</sub>//CC/CNT-NiSe<sub>2</sub> cell were as follows: 88.176, 75.057, 38.4, 12.16, 2.4, and 1.4 F g<sup>-1</sup>. Finally, the *C<sub>s</sub>* of the CC/CNT-CuSe<sub>2</sub>//CC/CNT-CuSe<sub>2</sub> cell exhibited values of 74.028, 26.092, 4.834, 2.16, 0.9262, and 0.884 F g<sup>-1</sup>, respectively.

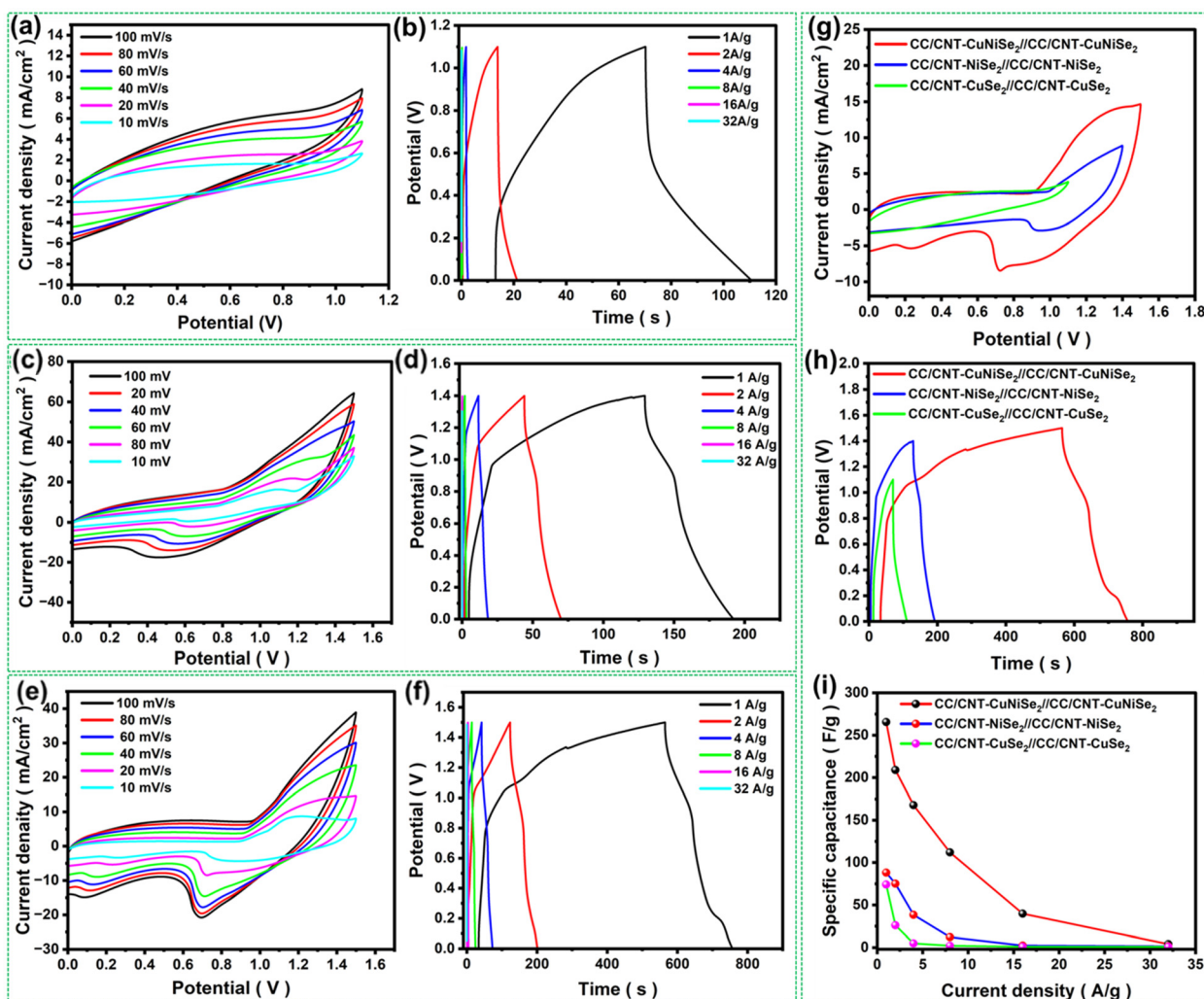


Fig. 7 (a), (c) and (e) CVs (b), (d) and (f) GCD profiles of (a) and (b) CC/CNT-CuSe<sub>2</sub>//CC/CNT-CuSe<sub>2</sub>, (c) and (d) CC/CNT-NiSe<sub>2</sub>//CC/CNT-NiSe<sub>2</sub> and (e) and (f) CC/CNT-CuNiSe<sub>2</sub>//CC/CNT-CuNiSe<sub>2</sub>. (g) CV difference of the HSCs at 20 mV scan rate. (h) GCD profile of all the HSCs at 1 A g<sup>-1</sup>. (i) Comparison of the *C<sub>s</sub>* of CC/CNT-CuNiSe<sub>2</sub>//CC/CNT-CuNiSe<sub>2</sub>, CC/CNT-NiSe<sub>2</sub>//CC/CNT-NiSe<sub>2</sub> and CC/CNT-CuSe<sub>2</sub>//CC/CNT-CuSe<sub>2</sub> at varying current densities.



The  $C_s$  values of the devices were plotted against the current densities, as shown in Fig. 7(i). At all current densities, the  $C_s$  values of the CC/CNT-CuNiSe<sub>2</sub>//CC/CNT-CuNiSe<sub>2</sub> device were shown to be three times greater than those of the CC/CNT-NiSe<sub>2</sub>//CC/CNT-NiSe<sub>2</sub> and CC/CNT-CuSe<sub>2</sub>//CC/CNT-CuSe<sub>2</sub> devices. It was observed that the  $C_s$  values of all devices consistently decreased from lower to higher current densities. Increased specific currents reduce the capacitance as they impede the movement of OH<sup>-</sup> ions to the surface, thereby decreasing ion penetration into the electrode's inner regions and elevating the Ohmic resistance. Next,  $E_d$  and  $P_d$  were evaluated using eqn (6) and (7), and the corresponding Rangone plot is shown in Fig. 7(b).

$$E_d \text{ (W h kg}^{-1}\text{)} = (C_s \times \Delta V^2 \times 1000)/7200 \quad (6)$$

$$P_d \text{ (W kg}^{-1}\text{)} = (3600 \times E_{den})/\Delta t \quad (7)$$

Here,  $E_d$  is energy density,  $P_d$  is the power density,  $\Delta t$  is the difference from the discharge time, and  $\Delta V$  is the potential window.

The performance of CC/CNT-CuNiSe<sub>2</sub>//CC/CNT-CuNiSe<sub>2</sub>, CC/CNT-NiSe<sub>2</sub>//CC/CNT-NiSe<sub>2</sub>, and CC/CNT-CuSe<sub>2</sub>//CC/CNT-CuSe<sub>2</sub> symmetric devices were assessed, and they exhibited high  $E_d$  and  $P_d$  values. The CC/CNT-CuNiSe<sub>2</sub>//CC/CNT-CuNiSe<sub>2</sub> device delivered 82.99 W h kg<sup>-1</sup> at 1511.35 W kg<sup>-1</sup> (1 A g<sup>-1</sup>) and 1.28 W h kg<sup>-1</sup> at 48 000 W kg<sup>-1</sup> (32 A g<sup>-1</sup>). Whereas, the CC/CNT-NiSe<sub>2</sub>//CC/CNT-NiSe<sub>2</sub> and CC/CNT-CuSe<sub>2</sub>//CC/CNT-CuSe<sub>2</sub> devices delivered 24.0, 12.44 W h kg<sup>-1</sup> at 1399.92, 1099.84 W kg<sup>-1</sup> (1 A g<sup>-1</sup>) and 0.381, 0.148 W h kg<sup>-1</sup> at 44 129.02, 38 057.14 W kg<sup>-1</sup> (32 A g<sup>-1</sup>). In comparison to CC/CNT-NiSe<sub>2</sub>//CC/CNT-NiSe<sub>2</sub> and CC/CNT-CuSe<sub>2</sub>//CC/CNT-CuSe<sub>2</sub>, the CC/CNT-CuNiSe<sub>2</sub>//CC/CNT-CuNiSe<sub>2</sub> device showed significantly high  $E_d$  and  $P_d$  values, and its energy-storage performance was better than the reported literature data, as presented in Table 1.

The stability study of the CC/CNT-CuNiSe<sub>2</sub>//CC/CNT-CuNiSe<sub>2</sub> hybrid symmetric device was done at 4 A g<sup>-1</sup> for 6000 consecutive GCD cycles. The device's specific capacitance retention and coulombic efficiency were plotted as a function of the cycles in Fig. 8(c) and (d). At the end of 6000 cycles of charge and discharge at a higher current density, the CC/CNT-CuNiSe<sub>2</sub>//CC/CNT-CuNiSe<sub>2</sub> device delivered a  $C_s$  of

101.3% with a coulombic efficiency of 93.63%, as measured using Equation S2. Initially, there was an increase in the capacitance of 115%, up to 1500 cycles. After 1500 cycles, the  $C_s$  became stable, and it was constant, with not much loss in  $C_s$ , which was projected to be 101.3% at the end of 4000 cycles. There was no loss in  $C_s$  observed up to 6000 cycles; however, since there was no proper wettability between the electrode and electrolyte at the beginning, fluctuations in specific capacitance may occur during the continuous cycling. Importantly, due to the participation of all the electrode materials at the start of the cycles, after certain periods, the degradation of the material can occur, which may lead to structural morphology changes. The comprehensive analysis of the  $C_s$ ,  $P_d$ ,  $E_d$ , and long cycle durability of CC/CNT-CuNiSe<sub>2</sub>//CC/CNT-CuNiSe<sub>2</sub> demonstrated significant support and enhancement, resulting in an effective electrochemical hybrid supercapacitor cell. Furthermore, the CC/CNT-CuNiSe<sub>2</sub>//CC/CNT-CuNiSe<sub>2</sub> HSC device was used to power a commercial light emitting diode (LED), which could be charged to 1.5 V, as shown in Fig. 8(e), confirming the potential use of device in a real-world application. The post-characterization of the HSD materials was performed by FESEM and XRD, as shown in Fig. S9 (a)–(d).† The result revealed that there was no significant morphological or structural changes compared to HSC materials before the long-time GCD analysis. Further, the self-discharging behaviour of the HSC was assessed after charging to 1.5 V, assuming that the relaxing phenomena had time constants of less than 1 h. Consequently, when the charging current was stopped, the decrease in voltage across the supercapacitor was only from the effect of self-discharge. Fig. S10† shows the self-discharge of the aforementioned supercapacitor at an ambient temperature of 25 °C and for an initial voltage of 1.5 V. It was observed that the device showed a 0.4 V loss after 5000 s and the device decay stabilized at 1.1 V, with less self-discharge. The performance of the device thus showed its suitability for use in energy-storage applications.

### 3.4. Electrochemical impedance spectroscopy (EIS)

EIS was performed to analyze all three electrodes, as shown in Fig. S8† and in the photos of the symmetric device in Fig. 8(f), from 0.01 Hz to 10<sup>5</sup> Hz, and the results were best fitted with the basic Randles circuit, as shown in Fig. S11† (inset) and

**Table 1** Comparison of  $C_s$ ,  $E_d$ , and  $P_d$  of CNT-CuNiSe<sub>2</sub> with various reported bimetallic selenide electrodes and their devices

Electrode material	Specific capacitance	Energy density (W h kg <sup>-1</sup> )	Power density (W kg <sup>-1</sup> )	Cyclic stability	$C_s$ retention	Ref.
CoNi-Se/rGO	2957 F g <sup>-1</sup>	73	1500	20 000	83%	58
Co-NiSe <sub>2</sub> /MXene	1394.8 F g <sup>-1</sup>	20	684	5000	67%	60
CF/Cu <sub>2</sub> S@Cu <sub>3</sub> Se <sub>2</sub> /P	1099 C g <sup>-1</sup>	41.1	480.4	10 000	90.2%	61
Co-Ni-Se/BWCF-160	3050 F g <sup>-1</sup>	49.7	1052	5000	93.3%	62
3DG/ZnSe-SnSe <sub>2</sub>	1515.2 F g <sup>-1</sup>	25.3	750	20 000	91.3%	63
Cu <sub>2</sub> Se <sub>4</sub> -Cu <sub>x</sub> Co <sub>1-x</sub> Se <sub>2</sub>	349.1 F g <sup>-1</sup>	26.84	700	5000	94.1%	64
Ni <sub>2</sub> CoS <sub>4</sub> @(NiCo)Se <sub>2</sub>	6054 mF cm <sup>-2</sup>	53	480	10 000	84.0%	37
ZnSe/MnSe	1439.98 F g <sup>-1</sup>	56.17	265	5000	65	65
NiMoSe <sub>2</sub>	480 F g <sup>-1</sup>	44.04	2000.1	15 000	99.4%	66
rGO-MnSe <sub>2</sub> /CoSe <sub>2</sub>	1214 F g <sup>-1</sup>	49.7	888	5000	88%	67
CNT-CuNiSe <sub>2</sub>	957.06 F g <sup>-1</sup>	82.99	1511.35	6000	101.3%	This work



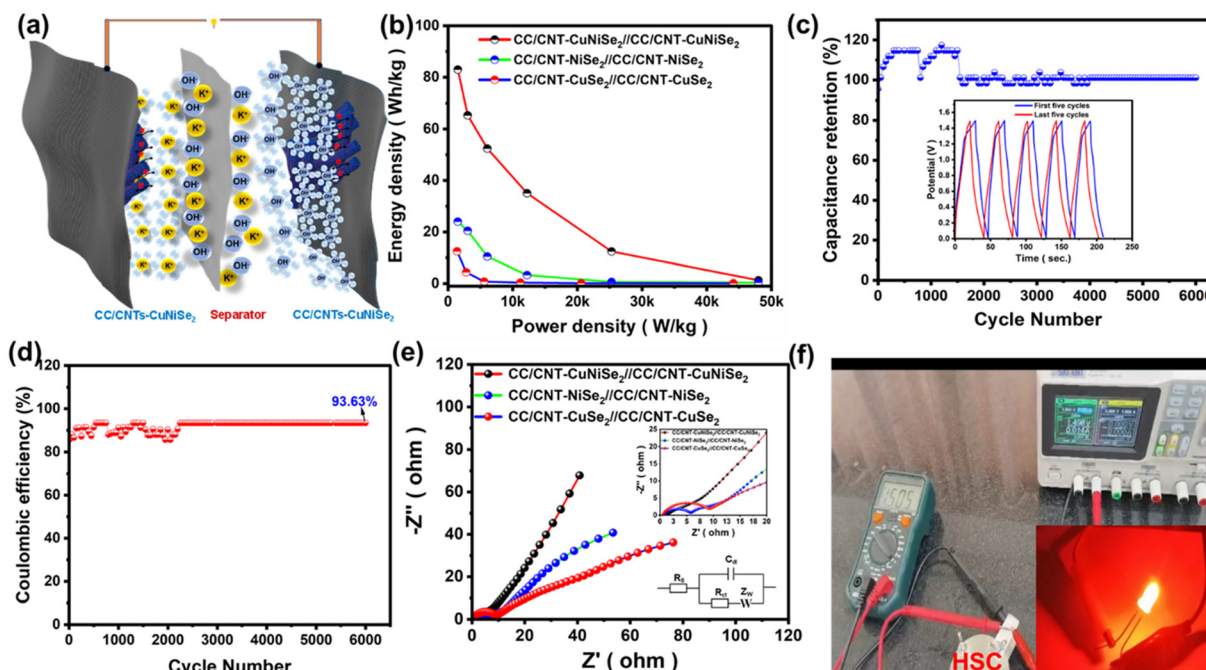


**Fig. 8** (a) Graphical representation of the two-electrode system. (b) Specific energy versus specific power plots of the HSCs. (c)  $C_s$  retention of the symmetric SC  $CC/CNT-CuNiSe_2//CC/CNT-CuNiSe_2$ ; inset shows the initial and final GCD consecutive cycles of 6000 cycles of GCD at  $4 A g^{-1}$ . (d) Coulombic efficiency of HSC over the period of 6000 cycles. (e) Electrochemical impedance spectra of all three HSCs in 6 M KOH solution. (f)  $CC/CNT-CuNiSe_2//CC/CNT-CuNiSe_2$ -powered HSC device illuminating a 1 V LED.

Fig. 8(f inset). The  $R_{ct}$ ,  $R_s$ , and  $W$  values of  $CNT-CuNiSe_2$  were 0.1279 m $\Omega$ , 13.8  $\Omega$ , and 0.00072  $\Omega$ ; while for  $CNT-NiSe_2$ , the values were 0.135 m $\Omega$ , 14.2  $\Omega$ , and 0.00082  $\Omega$ . Finally, the  $CNT-CuSe_2$  electrodes had values of 15.57  $\Omega$ , 0.143 m $\Omega$ , and 0.011  $\Omega$ , respectively. Similarly, EIS analysis was carried out for  $CC/CNT-CuSe_2//CC/CNT-CuSe_2$  (17.4  $\Omega$ , 0.9713  $\Omega$  and 0.0334  $\Omega$ ),  $CC/CNT-NiSe_2//CC/CNT-NiSe_2$  (8.04  $\Omega$ , 0.6791  $\Omega$  and 0.04015  $\Omega$ ) and  $CC/CNT-CuNiSe_2//CC/CNT-CuNiSe_2$  (2.359  $\Omega$ , 0.6047  $\Omega$  and 0.03579  $\Omega$ ) devices. It was observed that the  $CC/CNT-CuNiSe_2//CC/CNT-CuNiSe_2$  device exhibited low resistance parameters. From this study, it is evident that  $CC/CNT-CuNiSe_2//CC/CNT-CuNiSe_2$  SC had effectively low  $R_{ct}$ ,  $R_s$ , and  $W$  values, which are favourable for enhanced charging and discharging of the SC, thus increasing the coulombic efficiency.

## 4. Conclusions

We successfully synthesized CNT-modified bimetallic  $CuNiSe_2$  through an *in situ* reaction in a one-pot process utilizing liquid-phase reduction method, which is an efficient and cost-effective approach for the development of bimetallic selenides as energy-storage device materials. We believe this method significantly enhances the electrochemical performance using the one-pot synthesis protocol. In addition, this synthesis procedure helps form uniform  $CuNiSe_2$  nanoparticles distributed over the walls of the CNTs, maintaining the synergistic benefits from the pi-cloud of the carbon nanotubes. As a

result, increases in high electrochemical storage performance and the unique faradaic characteristics have been observed in cyclic voltammetry and charge-discharge behavior analyses, including excellent electrical conductivity of the aqueous electrolyte and redox activity, leading to an enhanced specific capacitance of 957.06  $F g^{-1}$  at a current density of 1  $A g^{-1}$  for the  $CNT-CuNiSe_2$  electrode. The  $CC/CNT-CuNiSe_2//CC/CNT-CuNiSe_2$  HSC demonstrated a capacitance of 265.586  $F g^{-1}$  at 1  $g^{-1}$ , achieving a capacitance retention of 101.3% and a coulombic efficiency of 93.63% after 6000 GCD cycles. The constructed  $CC/CNT-CuNiSe_2$  HSC exhibited remarkable performance, reaching a high energy density of 82.99  $W h kg^{-1}$  alongside a power density of 1511.35  $W kg^{-1}$ , with the capability to operate in the potential range of 0 to 1.5 V. Creating these materials using economical and eco-friendly methods would greatly benefit energy-storage applications in both industrial and commercial sectors.

## Author contributions

The manuscript was written with contributions from all authors, and all authors have approved the final version of the manuscript.

## Data availability

Data files can be shared upon reasonable request.



## Conflicts of interest

The authors declare that there are no financial interests or personal relationships that could have influenced the work presented in this paper.

## Acknowledgements

Soumyajit Jana and K. Yugender Goud would like to express their gratitude to the Department of Science and Technology, Science and Engineering Research Board (DST-SERB/RJF/2021/000113, Ramanujan Award), New Delhi, India, and the Indian Institute of Technology Palakkad, Seed Grant Project (2024-254-CHY-YGK-SGP-SP) for their financial support and research facilities. The authors also acknowledge the Central Instrumentation Facility at IIT Palakkad for chemical and material characterizations, as well as the SRM Central Instrumentation Facility (SCIF) for TEM characterization. The ToC and Fig. 8a were created with Blender *via* Blender Foundation and VESTA (K. Momma and F. Izumi, "VESTA 3 for three-dimensional visualization of crystal, volumetric and morphology data," *J. Appl. Crystallogr.*, 2011, **44**, 1272–1276).

## References

- 1 A. Russo, M. Costanzo and A. Cavallo, 2022 5th Int. Conf. Mechatronics, Robot. Autom. ICMRA 2022, 2022, 64–68.
- 2 Y. Liu, S. P. Jiang and Z. Shao, *Mater. Today Adv.*, 2020, **7**, 100072.
- 3 C. Zhong, Y. Deng, W. Hu, J. Qiao, L. Zhang and J. Zhang, *Chem. Soc. Rev.*, 2015, **44**, 7484–7539.
- 4 Z. Lin, E. Goikolea, A. Balducci, K. Naoi, P. L. Taberna, M. Salanne, G. Yushin and P. Simon, *Mater. Today*, 2018, **21**, 419–436.
- 5 S. Karingula, S. Kumari, Y. Goud Kotagiri, L. Malyala and K. Vengatajalabathy Gobi, *Small*, 2025, **21**, 2408899.
- 6 H. Jabraoui, D. Pech, M. D. Rouhani, C. Rossi and A. Esteve, *J. Energy Storage*, 2024, **98**, 112926.
- 7 S. Mothkuri, S. Chakrabarti, H. Gupta, B. Padya, T. N. Rao and P. K. Jain, *Mater. Today: Proc.*, 2018, **26**, 142–147.
- 8 T. Hao, Y. Liu, G. Liu, C. Peng, B. Chen, Y. Feng, J. Ru and J. Yang, *Energy Storage Mater.*, 2019, **23**, 225–232.
- 9 L. Kang, S. Liu, Q. Zhang, J. Zou, J. Ai, D. Qiao, W. Zhong, Y. Liu, S. C. Jun, Y. Yamauchi and J. Zhang, *ACS Nano*, 2024, **18**, 2149–2161.
- 10 H. S. Shahidani, M. Seifi and M. Bagher Askari, *Inorg. Chem. Commun.*, 2024, **170**, 113218.
- 11 C. Miao, X. Xiao, Y. Gong, K. Zhu, K. Cheng, K. Ye, J. Yan, D. Cao, G. Wang and P. Xu, *ACS Appl. Mater. Interfaces*, 2020, **12**, 9365–9375.
- 12 C. Lu, Y. Yang, S. Li and M. Zhu, *Mater. Chem. Front.*, 2024, **8**, 2282–2292.
- 13 M. Aman, V. Sharma and S. Omar, *Appl. Surf. Sci.*, 2024, **670**, 160611.
- 14 Y. Dong, T. Li, H. Su, X. Zhang and J. Zhang, *J. Hazard. Mater.*, 2024, **477**, 135281.
- 15 K. Zhang, Y. Li, S. Deng, S. Shen, Y. Zhang and G. Pan, *ChemElectroChem*, 2019, 3530–3548.
- 16 Y. Gu, Y. Katsura, T. Yoshino, H. Takagi and K. Taniguchi, *Sci Rep.*, 2015, 1–9.
- 17 N. S. Arul and J. I. Han, *Mater. Lett.*, 2016, **181**, 345–349.
- 18 G. P. Patil, C. D. Jadhav, S. Lyssenko, A. Borenstein and R. Minnes, *J. Mater. Chem. C*, 2024, 14404–14420.
- 19 T. Chen, S. Li, J. Wen, P. Gui, Y. Guo, C. Guan, J. Liu and G. Fang, *Small*, 2018, **14**, 1–8.
- 20 M. Amiri, A. Mohammadi Zardkhouhou, S. S. Hosseiny Davarani, M. Maghsoudi and M. K. Altafi, *Sustainable Energy Fuels*, 2022, **6**, 3626–3642.
- 21 Z. Li, M. Tian, Y. Chen, Y. Liu, Y. Cai and W. Wei, *Ceram. Int.*, 2021, **47**, 12623–12630.
- 22 Y. Yang, L. Liu, S. Li and M. Zhu, *ACS Appl. Energy Mater.*, 2024, **7**, 7307–7315.
- 23 M. Molaei, M. Abdollahi, A. M. Zardkhouhou and S. S. H. Davarani, *J. Energy Storage*, 2024, **85**, 111079.
- 24 Q. Lu, T. Zhou, M. Chen, J. Zhao, H. Sun, B. Li, B. Zi, J. Zhang, Z. Zhu and Q. Liu, *ACS Energy Lett.*, 2024, 145–155.
- 25 G. Zhang, H. Xuan, J. Yang, R. Wang, Z. Xie, X. Liang, P. Han and Y. Wu, *J. Power Sources*, 2021, **506**, 230255.
- 26 S. H. Lee, J. H. Kim and J. R. Yoon, *Sci. Rep.*, 2018, **8**, 1–9.
- 27 Y. Yang, Y. Ma, C. Lu, S. Li and M. Zhu, *Green Chem.*, 2023, **25**, 10209–10234.
- 28 B. Liu, Y. Ye, M. Yang, Y. Liu, H. Chen, H. Li and W. Fang, *Adv. Funct. Mater.*, 2024, **2310534**, 1–10.
- 29 B. Liu, L. Zhao, Y. Liu, H. Chen, H. Li, M. Yang and J. Qiu, *Adv. Mater.*, 2025, **2419124**, 1–10.
- 30 H. Ding, S. Zhao, X. Wang, C. Qian, T. Zou, X. Li, H. Li, F. Jiang, Y. Liu, H. Cao, Z. Fang and Y. Zhu, *Colloids Surf., A*, 2023, **668**, 131462.
- 31 Y. Peng, M. Wei, D. Zhang, X. Liu, X. Xiong, W. Gao, W. Fan, H. Yang, Q. Zhou, T. Wang, F. Wang, Y. Ma, Y. Zhong, X. B. Cheng, Z. Zhu, J. He and Y. Wu, *Nano Energy*, 2024, **130**, 110077.
- 32 M. Liu, J. Xu, L. Shao, X. Shi, C. Li and Z. Sun, *Chem. Commun.*, 2024, **60**, 6860–6872.
- 33 G. Li, Y. Tang, S. Cui, H. Chen, H. Chong and L. Han, *Adv. Funct. Mater.*, 2024, **2401586**, 1–10.
- 34 B. G. Amin, J. Masud and M. Nath, *RSC Adv.*, 2019, 37939–37946.
- 35 J. Yan, L. Rasenthiram, H. Fang, R. Tjandra, L. Wang, L. Wang and Y. Zhang, *Ionics*, 2019, 675–683.
- 36 N. Bibi, Y. Xia, S. Ahmed, Y. Zhu, S. Zhang and A. Iqbal, *Ceram. Int.*, 2018, **44**, 22262–22270.
- 37 L. Duan, H. Fu, H. Guo, H. Sun, Q. Zhang, J. Xu and J. Liu, *Appl. Surf. Sci.*, 2024, **648**, 158966.
- 38 A. Ullah, K. Tahir, H. M. A. Hassan, K. Albalawi, Q. Ullah, A. Khan, M. M. Moharam, S. Latif, M. S. Refat and A. Mohammed, *J. Electroanal. Chem.*, 2022, **920**, 116624.



- 39 S. Hussain, M. Sufyan, S. Asim, A. Shaheen, A. Jabbar, Y. Abbas, N. Ullah, A. Iqbal, M. Wang, G. Qiao and S. Yun, *Ceram. Int.*, 2020, **46**, 6406–6412.
- 40 Y. Lu, X. Liu, W. Wang, J. Cheng, H. Yan, C. Tang, J. K. Kim and Y. Luo, *Sci. Rep.*, 2015, **5**, 1–11.
- 41 H. Charles, P. J. Chengula, H. Oh and C. S. Lee, *Surf. Interfaces*, 2024, **52**, 104838.
- 42 H. Li, H. Zu, Q. Li, J. Yang, W. Qu and Z. Yang, *Environ. Sci. Technol.*, 2022, **56**, 575–584.
- 43 B. Jansi Rani, G. Ravi, R. Yuvakkumar, B. Saravanakumar, M. Thambidurai, C. Dang and D. Velauthapillai, *ACS Omega*, 2020, **5**, 14702–14710.
- 44 M. Farbod, S. K. Tadavani and A. Kiasat, *Colloids Surf., A*, 2011, **384**, 685–690.
- 45 Z. Li, X. Ma, L. Wu, H. Ye, L. Li, S. Lin, X. Zhang, Z. Shao, Y. Yang and H. Gao, *RSC Adv.*, 2021, **11**, 6842–6849.
- 46 W. Zhang, W. Yang, H. Zhou, Z. Zhang, M. Zhao, Q. Liu, J. Yang and X. Lu, *Electrochim. Acta*, 2020, **357**, 136855.
- 47 P. A. Shinde, N. R. Chodnakar, Mohammad A. Abdelkarrem, Swati J. Patil, Y. K. Han, K. Elsaid and A. G. Olabi, *Small*, 2022, **18**, 2200248.
- 48 T. Li, Q. Zhang, X. H. Wang, J. Luo, L. Shen, H. C. Fu, F. Gu, N. B. Li and H. Q. Luo, *Nanoscale*, 2021, **13**, 17846–17853.
- 49 F. Ming, H. Liang, H. Shi, X. Xu, G. Mei and Z. Wang, *J. Mater. Chem. A*, 2016, **4**, 15148–15155.
- 50 S. Karingula, S. Kumari, Y. Goud Kotagiri and K. Vengatajalabathy Gobi, *Small*, 2024, 2400812.
- 51 J. Zhou, M. Chen, T. Wang, S. Li, Q. Zhang, M. Zhang, H. Xu, J. Liu, J. Liang, J. Zhu and X. Duan, *iScience*, 2020, **23**, 100919.
- 52 Q. Han, W. Zhang, L. Zhu, M. Liu, C. Xia, L. Xie, X. Qiu, Y. Xiao, L. Yi and X. Cao, *ACS Appl. Mater. Interfaces*, 2024, **16**, 6033–6047.
- 53 F. Jin, M. Li, L. Xie and J. Jiang, *J. Power Sources*, 2021, **514**, 230587.
- 54 S. Kondrat, C. R. Pérez, V. Presser, Y. Gogotsi and A. A. Kornyshev, *Energy Environ. Sci.*, 2012, **5**, 6474–6479.
- 55 A. Iakunkov, V. Skrypnychuk, A. Nordenström, E. A. Shilayeva, M. Korobov, M. Prodana, M. Enachescu, S. H. Larsson and A. Vtalyzin, *Phys. Chem. Chem. Phys.*, 2019, **21**, 17901–17912.
- 56 Z. Andikaey, A. A. Ensafi, B. Rezaei and J. S. Hu, *Electrochim. Acta*, 2022, **417**, 140338.
- 57 Q. Wang, X. Tian and D. Zhang, *Matlet.*, 2020, **276**, 8–11.
- 58 E. Aboelazm, C. S. Khe, K. F. Chong, M. S. Mohamed Saheed and M. B. Z. Hegazy, *ACS Appl. Mater. Interfaces*, 2024, **16**, 15011–15022.
- 59 J. Balamurugan, T. T. Nguyen, V. Aravindan, N. H. Kim, S. H. Lee and J. H. Lee, *Nano Energy*, 2019, **65**, 103999.
- 60 M. Patel, S. Patel, K. Mahabari, R. Mohili, A. H. Jadhav, M. Sharma, K. Lee and N. K. Chaudhari, *ACS Appl. Nano Mater.*, 2024, **7**, 28172–28185.
- 61 H. Fu, A. Zhang, H. Guo, L. Duan, F. Jin, H. Zong, X. Sun and J. Liu, *ACS Appl. Mater. Interfaces*, 2023, **15**, 8169–8180.
- 62 M. Gao, Y. Xue, Y. Zhang, C. Zhu, H. Yu, X. Guo, S. Sun, S. Xiong, Q. Kong and J. Zhang, *Inorg. Chem. Front.*, 2022, **9**, 3933–3942.
- 63 T. Zhao, G. Feng, L. Zhou, X. Wang, X. Li, F. Jiang, H. Li, Y. Liu, Q. Yu, H. Cao, Y. Xu and Y. Zhu, *ACS Appl. Nano Mater.*, 2024, **7**, 13434–13446.
- 64 X. Yang, X. Chen, H. Cao, C. Li, L. Wang, Y. Wu, C. Wang and Y. Li, *J. Power Sources*, 2020, **480**, 228741.
- 65 M. Hussain, B. M. Alotaibi, A. W. Alrowaily, H. A. Alyousef, M. F. Alotiby, M. Abdullah, A. G. Al-Sehemi, A. M. A. Henaish, Z. Ahmad and S. Aman, *J. Phys. Chem. Solids*, 2024, **188**, 111919.
- 66 J. J. J. Kamaraj, P. Annamalai, S. Perumal, S. P. Muthu and R. Perumalsamy, *J. Energy Storage*, 2023, **73**, 109262.
- 67 T. S. Krishnan, P. S. Babu, M. Praveen and V. Janakiraman, *J. Electron. Mater.*, 2024, **53**, 5273–5285.

